Available online at www.sciencedirect.com
ScienceDirect
Trans. Nonferrous Met. Soc. China 33(2023) 3282−3294
Transactions of Nonferrous Metals Society of China
www.tnmsc.cn

Effect of plastic strain under roller bending on fatigue properties of extruded 6063 T66 aluminium alloy profile

Tomasz TOMASZEWSKI, Michał STOPEL, Andrzej SKIBICKI, Jan SEYDA, Tomasz PIĄTKOWSKI

Faculty of Mechanical Engineering, Bydgoszcz University of Science and Technology, Bydgoszcz, Poland

Received 24 May 2022; accepted 20 September 2022

Abstract: The tensile plastic strain of material sampled from profiled areas under roller bending and pre-strained material was analyzed. The experimental data of high-cycle fatigue were approximated by a probabilistic Weibull cumulative distribution (*P*−*S*−*N* curve). The fatigue life prediction model was implemented for numerical simulations of roller bending in the LS-Dyna solver and experimental data. The cyclic behaviour of the material shows a decrease in the fatigue life distribution with increasing static failure levels. The fractographic analysis of the fracture surface shows an increased level of intergranular cracking for the tensile pre-strain as a result of the dislocation accumulation in the neighbourhood of grain boundaries. The estimation results of the proposed model show good correlation of probabilistic scatter bands (error below 10%).

Key words: 6063 aluminium alloy; pre-strain; high-cycle fatigue; *P*−*S*−*N* curve; Weibull distribution

1 Introduction

The manufacture of spatial aluminium profile structures determines the use of the three-roller bending. The process is one of the most widely used profile bending procedures due to its high flexibility and relatively low machine costs [1]. An advantage of the process is the minimization of the remaining straight section, which reduces material waste and subsequent machining costs [2]. About other bending methods, this forming process results in a reduced strain of the cross-section, achieving higher actual deformations with a smooth change of the bending radius. The high efficiency of the method is a result of the local yielding of the bending section by the longitudinal rolling process. WELO and WIDERØE [3] studied the forming mechanism in combination with models to optimize tool design and technology, improving the dimensional accuracy of the component.

The effects of selected parameters on the forming mechanisms in terms of the geometric response of the profile to given bending conditions are commonly explained by analysis of numerical methods. FENG and CHAMPLIAUD [4] obtained a good prediction of the roll position using the finite element method with shell elements. YANG et al [5] studied the curvature distribution by feedback control in a FEM simulation. The roll motion is iteratively modified based on fuzzy reasoning using the calculated curvature distribution during bending at each deformation step. SHIM et al [6] analysed two-stage forming by adjusting the pre-bending radius to minimise the deformation of the profile cross-section.

The profile forming during the production cycle requires the application of a large permanent deformation exceeding the elastic limit of the material. The release of the applied moment causes an elastic linear recovery and permanent plastic deformation. The process determines the local

Corresponding author: Tomasz TOMASZEWSKI, E-mail: tomaszewski@pbs.edu.pl
DOI: 10.1016/S1003-6326(23)66333-2

residual stress. The second area of numerical simulation concerns material condition assessment. HUDOVERNIK et al [7] numerically studied the stress and strain state to understand the spring-back, section deformation and residual stress. CHIEW et al [8] estimated the residual stresses of numerical modelling of the rolling process. The bending factor, yield strength, aspect ratio and section thickness ratio significantly affect the residual stresses.

The aluminium 6000 series alloys with excellent formability are commonly used for bending thin-walled extruded parts. The final state of the material depends on the thermo-mechanical process, final microstructure, crystallographic texture, and loading history. The mechanical properties depend on the size of the precipitates formed during the artificial ageing at 160−180 °C [9−11]. The formability and strain hardening decrease with increasing ageing time [12]. The elongation of the alloy is significantly affected by the grain refining effect from recrystallization [13]. The work hardening changes the shape of the stress−strain curve for axial loading. The plastic strain increases the yield strength and ultimate tensile strength while reducing material elongation. An increase in dislocation density due to the multiplication or formation of new dislocations is observed [14−16]. For the cyclic properties of aluminium alloys, the fatigue crack initiation is related to metallurgical micro properties (micro-porosity, constituent particles, and grain structure). The fatigue life for uniaxial tension decreases with increasing yield strain [17]. The dislocation localisation for the strained material is observed mainly in the slip bands [18]. KIM et al [19] studied the effect of applied bending overload moment on fatigue behaviour. The presence of the tensile residual stress accelerates crack initiation and growth. FROUSTEY and LATAILLADE [20] showed no effect of pre-strain on the residual fatigue life behaviour.

The paper concerns the analysis of the effect of plastic pre-strain on the fatigue properties of the extruded EN AW 6063 T66 aluminium alloy profile. The objective of the study is determined by the variable state of material strain in profiles under roller bending. The material tests carried out were estimated using a probabilistic model of the Weibull cumulative distribution and fractographic analysis of the fracture surface. The strain level during the profile forming process was modelled numerically using LS-Dyna solver. The procedure determined the maximum strain in the profile and estimated the probabilistic fatigue life scatter bands.

2 Experimental

2.1 Material

The tested profile is made from EN AW 6063 T66 aluminium alloy (AlMgSi0.5F25). The material is recommended for structural applications in extruded and cold-drawn products. The alloy is used for profiles with complex shapes and is particularly suitable for anodizing and similar finishing processes. The hardened state of the material (T66) was achieved by cooling down from the forming operation at an elevated temperature and artificially aged to a state with improved mechanical properties. The profile is coated with an anode. The chemical composition of the material was determined using a JEOL 6480LV scanning microscope and an EDS detector for X-ray microanalysis. Table 1 summarizes the composition of elements compared to standard requirements [21]. The values are comparable.

The microstructure was analysed in the longitudinal direction of the profile. The metallographic microsections were processed using conventional methods. The surfaces were ground and polished with a diamond slurry with a gradation of 1 μm on a FORCIPOL 202 metallographic grinder-polisher. The polished surfaces of the specimens were etched with Keller's reagent consisting of 0.5 mL HF (40%), 1 mL HCl (31%), 1.5 mL HNO_3 (80%) and 47 mL H_2O for 240 s at room temperature. The microstructure of the material

Table 1 Chemical composition of tested aluminium alloy (wt.%)

Item	Si	Fe	Cu	Mn	Mg	Cr	Zn	Ti	Al
Standard requirement [21]	0.20−0.60	0.35	0.10	0.10	0.45−0.90	0.10	0.10	0.10	Rest
Measured value	0.39	0.32	0.06	0.10	0.81	0.09	0.11	0.09	Rest

was evaluated using a JEOL 6480LV scanning microscope. Figure 1 shows the microstructure of as-received EN AW 6063 T66 material.

The particles are arranged in streams along the direction of pulling. From the analysis of EDS chemical composition and literature data [22,23], it can be concluded that the particles are AlFeSi. The particle size was estimated to be around 2 μm. Due to the recrystallization of grains under roller bending, grain directionality is not observed for the strained material. The analysis showed no significant differences in deformation and grain size as a function of pre-strain. The conclusion is consistent with other studies [15]. The average grain size is equal to 75 μm for all material states. The measurements were made in accordance with ASTM E112 [24] using the method of grains intercepted by the line.

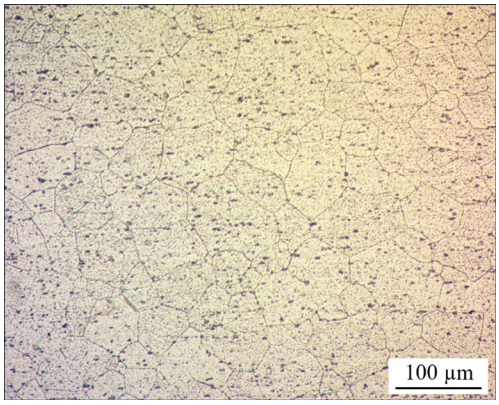

Fig. 1 Microstructure of as-received EN AW 6063 T66 material

2.2 Specimens and test procedure

Figure 2(a) shows the cross-sectional geometry of the tested aluminium profile. The straight sections of the anodized profile were delivered from the manufacturer. Figure 2(b) shows the actual top view of the profile after the bending process. The straight section visible on the right is tangentially formed into an arc with a radius of 2150 mm. The rolled surface is the long side of the profile (120 mm). No heat treatment was applied to the profile during or after the roller bending process. The profile was applied to the support structure of a cross-belt sorter. The machine was used to automate logistical processes in intelligent warehouses. The sorter track is a closed loop used to transport cross conveyors in the progressive movement. The modular geometry of the track, assembled from straight sections and curves, necessitates the use of space profiles.

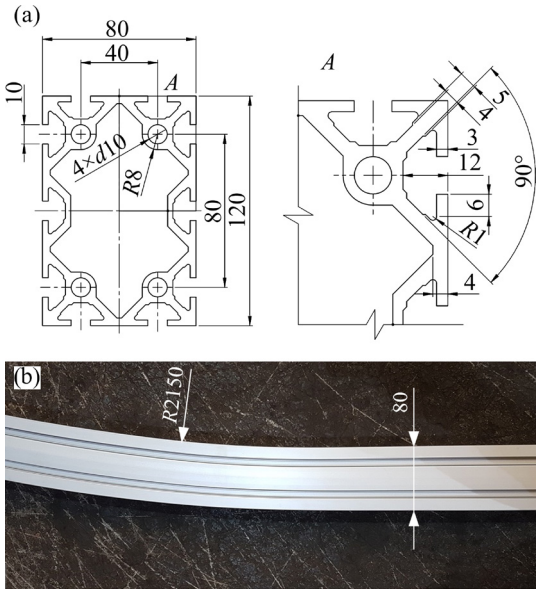

Fig. 2 Tested aluminium profile: (a) Cross-sectional geometry; (b) Actual view (unit: mm)

All tests were carried out using an Instron ElectroPuls E3000 dynamic and fatigue testing machine with an electrodynamic drive and a force gauge with a measuring range of ±5 kN, an Instron 2620 axial strain gauge with a 12.5 mm base and an elongation range of ±5 mm. The mechanical properties were identified by a static tensile test in accordance with ISO 6892 [25]. The high-cycle fatigue tests under axial load were carried out in accordance with the following standards [26,27]. A symmetrical sinusoidal cycle (stress ratio, r=−1) with 40 Hz was applied. The study aim is to determine the S–N curves for the load-controlled test. The end criterion of the fatigue test is the macro-cracking of the specimen.

The failure surface was analysed based on the fractography of the tested specimens. The cracks were analysed using a JEOL 6480LV electron scanning microscope in a secondary electrons mode (SEM). The observations were performed at 20 kV acceleration voltage.

Figure 3 shows the dimensions and geometry of specimens sampled from two different regions of the aluminium profile. All specimens were machined while maintaining the constant technological parameters. Figure 4 shows the distribution of strain in relation to the neutral axis (ε_x). The tensile strain sampling location ($\varepsilon_{t,p}$) was determined by the

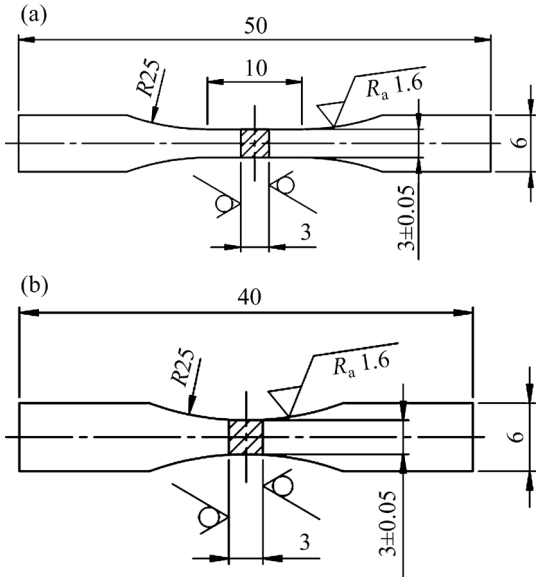

Fig. 3 Dimensions and geometry of unnotched specimen for monotonic tensile testing (a) and fatigue testing (b) (unit: mm)

highest yield strain occurring in the extreme fibres of the profile and technological possibilities of sampling. ε_0 and pre-strain of 2% ($\varepsilon_{t,2\%}$) of the as-received material were tested for specimens from a straight section. All specimens were located at the outer surface of the profile groove. The identified sampling location and the limited material volume resulting from the shape and dimensions of the profile (Fig. 2(a)) determine the requirement for testing on miniaturized specimens. The identification of test methodology for small specimen and extruded profiles was provided in the literature [28]. The development of fatigue property identification procedures has been discussed more extensively at periodic small specimen test technique conferences [29]. The miniaturization of specimens has a potential risk of data estimation errors resulting from size effects. The extrapolation of test results from the laboratory specimen sizes to the real object (profile) determines the implementation of the analytical models [30].

2.3 Numerical simulation conditions

The local strain in the aluminium profile under roller bending was determined numerically. The process simulations were carried out using the LS-Dyna explicit finite element solver. The explicit finite element method was commonly used for solving highly nonlinear problems such as those whose strains and deformation are large [31,32] or due to the boundary condition nonlinearity. There are both mentioned types of nonlinearity problems in the process under consideration of this study. The pre- and post-processor LS-PrePost software was used.

The aluminium profile of the total length of 2000 mm was discretized by 4-node shells under-integrated elements with Belytschko-Tsay formulation (*ELFORM type 2). Since those are under-integrated elements, they may be too soft in certain situations. To prevent that problem warping, the stiffness control card was introduced (*CONTROL_SHELL_BWC=2), and hourglass control was set to stiffness based on hourglass control with a coefficient of 0.1 (*HOURGLASS=4). To obtain the correct calculation results, the size of the elements was selected based on the mesh sensitivity investigation. This allowed to find a compromise between the permissible error and a significant reduction of the calculation time. The most compelling results were acquired with an element size of 3 mm (ES3). In that case, calculation time of a single case was 48 h. Ultimately, the element size was set to 6 mm (ES6). It has notably reduced computation time to 8 h with the difference of 10% in reaction force. The contact interfaces, element

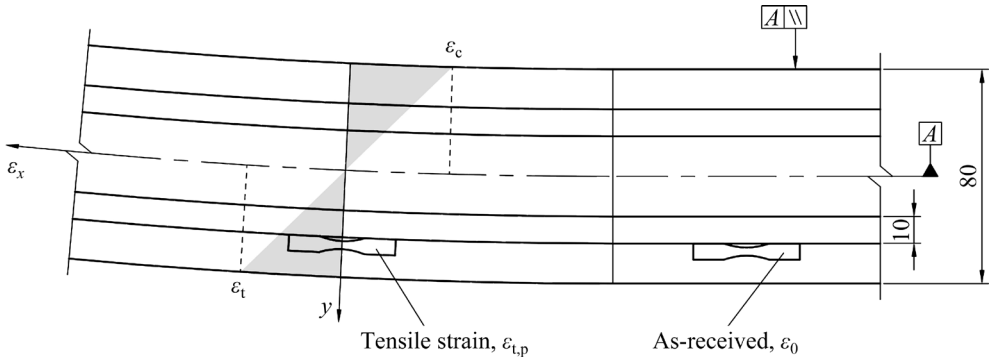

Fig. 4 Sampling scheme for extruded aluminium profile (unit: mm)

sizes, and material models were equal in every case, and the compromise described was found to be acceptable.

Figure 5 shows the geometry of the model with boundary conditions. The thickness of the surface elements corresponded to the real geometry of the profile, as shown in Fig. 2(a). The problem was modelled taking into account the symmetry to the plane x–z. All nodes lying on the symmetry plane were fixed in one translational degree of freedom along the y-axis and two rotational degrees of freedom around the z- and x-axis. There was a node, in the centre of gravity for each roller, connected to the roller nodes with the *CONTACT_NODAL_RIGID_BODY (*CNRB). For two stationary rollers, this node was fixed in all degrees of freedom. The bending roller displacement of the node in the centre of gravity was driven by a curve along the z-axis. Additionally, the node was rotated around the y-axis in a local coordinate system with a velocity (ω_r) of 1.15 rad/s. The rotation of the bending roller and the friction between the roller and the aluminium alloy caused the profile to move along the x-axis (f_p). The results of the numerical rolling bending process were obtained for one profile pass. For all the parts, the *PLASTIC_KINEMATIC (*Mat_24) material model allowing for plastic deformation was used. The corresponding variable values were introduced into the material models depending on the material used for the part (roller–steel, profile–aluminium). For the aluminium, instead of tangent modulus value, the experimental ε–σ curve for the as-received material was used.

3 Results and discussion

3.1 Mechanical properties

The strength characteristics in the elastic–plastic loading region of aluminium alloy are described by the nonlinear Ramberg-Osgood equation according to Eurocode 9 [33]. The analytical model determines the modulus of elasticity and strain hardening. Under monotonic loading conditions, the stress–strain function is described by continuous region-dependent models (elastic and plastic). Each material behaviour region is represented by model parameters, providing continuity at the boundary points. The general form of the model is presented as

$$\varepsilon=\frac{\sigma}{E}+\varepsilon_{\mathrm{e}}\left(\frac{\sigma}{R_{\mathrm{e}}}\right)^{n} \tag{1}$$

where ε is the total strain, σ is the stress, E is the modulus of elasticity, R_e is the conventional limit of elasticity (stress estimated by the 0.2% offset method), ε_e is the residual strain corresponding to the stress R_e, and n is the exponent characterizing the degree of hardening of the curve. The exponent n is determined from the Eq. (2):

$$n=\frac{\ln(\varepsilon_{\mathrm{e}}/\varepsilon_x)}{\ln(R_{\mathrm{e}}/R_x)} \tag{2}$$

where R_x is the second reference stress, and ε_x is the residual strain corresponding to the stress R_x. The selection of the stress R_x determines the range of strains corresponding to the studied phenomenon.

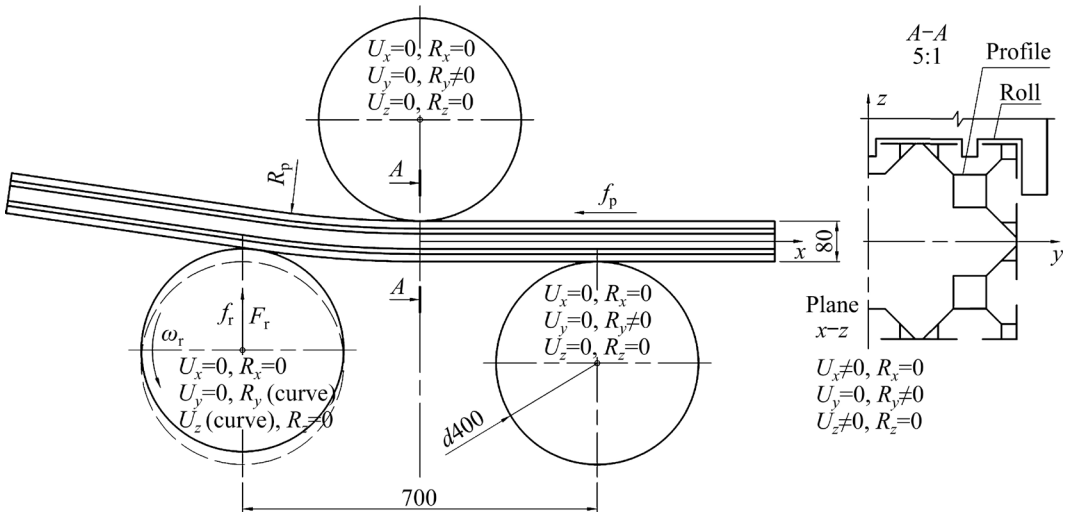

Fig. 5 Boundary conditions of numerical model (unit: mm)

The exponent n was determined for the range of elastic strain (ε_p, 0.1% offset) and yield strain (ε_{max}, ε offset for tensile strength R_m).

Figure 6 shows the engineering stress−strain curves for the profile regions. In the absence of a distinct yield stress, an approximation for a 0.2% displacement ($R_{0.2}$) was used. The elastic range is short. The curve above the strain for the tensile strength (R_m) determines a slight decrease in stress up to the macro-cracking of the specimen. Table 2 summarizes the mean values for the two specimens. The experimental data were above the minimum values recommended by Eurocode 9. The modulus of elasticity (E) was assumed to be 0.7×10^5 MPa. The selected mechanical properties were strain dependent. The strain hardening was observed for strain tension (R_m increase of 6.6 MPa, 2.6%) and yield strength ($R_{0.2}$ increase of 13.5 MPa, 5.9%). The values of longitudinal elongation and reduction of area are independent of strain.

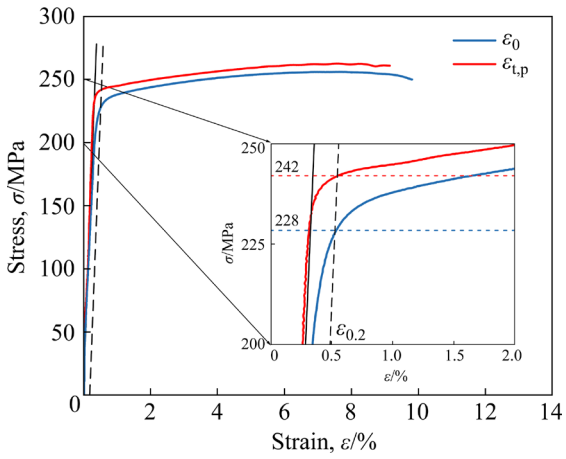

Fig. 6 Engineering stress−strain curves for various strains

The strain hardening can significantly affect the yield strength and tensile strength for the constant elongation of aluminium alloy. The variation of yield stress determines the exponent (n) of the Ramberg-Osgood equation. The as-received material (ε_0) has average values of 11.3 and 31.6 for the elastic and plastic range, respectively. The trend of the exponent (n) corresponds to the yield range. The strained material for the plastic range has values equal to 43.9 (38.9%) for strain tension. The exponent (n) determines the sharpness of the knee of the stress−strain curve. The higher values indicate lower strain hardening. The behaviour of EN AW 6063 T66 alloy is related to the increase in density or the formation of new dislocation loops and helical dislocations due to the local concentration. The crystal lattice distortions correlate with the level of strain input [14−16].

The material hardness was measured at five locations. Table 2 shows the average values for the data population. The tests were carried out using the Rockwell method. The experimental data were converted to the Brinell hardness scale (HB). The results showed slight variations, pointing to an increase in hardness for the strained material.

Table 2 Mechanical properties of EN AW 6063 T66 aluminium alloy

Parameter		Eurocode 9 [33]*	Specimen	
			ε_0	$\varepsilon_{t,p}$
Tensile strength, R_m/MPa		245	255.9	262.5
Yield strength, $R_{0.2}$/MPa		200	228.4	241.9
Longitudinal elongation, A/%		8	9.7	9.4
Reduction of area, Z/%		–	11.9	11.8
Exponent of Ramberg-Osgood law, n	Elastic range	–	11.3	63.7
	Plastic range	22	31.6	43.9
Hardness (HB)		–	73	75

* minimum value: Extruded profiles, thickness below 10 mm

3.2 *P*−*S*−*N* curves

The fatigue tests were carried out with controlled loading in the high-cycle fatigue range. Twelve specimens for each loading condition were tested (4 stress amplitude levels of 3 specimens each). The level of stress amplitude determines the fatigue life spread. The classical deterministic linear regression approach implies parallelism of the percentage curves. To avoid these contradictions, the experimental points were approximated by a probabilistic model for any nonparallel percentage curve (P−S−N). The model is based on a Weibull cumulative distribution function for a selected damage probability (P_f), as follows [34]:

$$P_f(N_f)=1-\exp\left[-\left(\frac{(N_f)-\lambda}{\delta}\right)^{\alpha}\right] \quad (3)$$

where N_f is the number of failure cycles, α is the shape parameter, δ is the scale parameter, and λ is the location parameter.

Figure 7(a) shows the P−S−N curves in a bi-logarithmic diagram determined for each loading

condition. The points are the number of cycles read from the measuring system for the stress amplitude (S_a). The dashed and dotted lines represent failure probabilities of 50%, 10%, and 90%, respectively. The fatigue curves for P_f equal to 50% and variable material conditions (ε_0, $\varepsilon_{t,p}$, $\varepsilon_{t,2\%}$) are characterized by parallel location relationships. The effect of plastic strain is independent of the stress amplitude level. A significant characteristic shift towards lower fatigue life is observed depending on the strain level. The 2% pre-strain test ($\varepsilon_{t,2\%}$) determines a larger fatigue life decrease than specimens sampled from a bent section of the profile ($\varepsilon_{t,p}$). The spread of data is typical of high-cycle fatigue tests.

Figure 7(b) shows the cumulative Weibull distribution for the extreme range of stress amplitude levels tested, S_a=180 MPa (solid line) and 120 MPa (dashed line). The points represent the estimated failure probability based on an approximation of the Weibull distribution. The decrease in fatigue life for variable material conditions ($\varepsilon_{t,p}$, $\varepsilon_{t,2\%}$) depends on the failure probability, especially for the low value (10%). The low level of stress amplitude and failure probability determines a slightly minor effect of plastic strain on the output.

Table 3 shows the calculated Weibull distribution parameters and the fatigue life for the selected failure probability. The scale parameter δ decreases with the level of pre-strain, pointing out that smaller fatigue life distributions are obtained for larger plastic strain. The variation obtained in the results is significantly noticeable.

3.3 Fracture surface morphology

Figure 8 shows SEM micrographs of the fracture surface of as-received material. The specimen tested at a stress amplitude of 180 MPa survived a number of cycles to failure N_f of 11879. Figure 8(a) shows the crack surface showing three typical areas: crack origin, propagation region, and failure region. The dashed line marks the boundary of the crack propagation region and failure region. All primary cracks are initiated directly or near the corner of the specimen (Fig. 8(b)). The behaviour is typical for this cross-section geometry. The local geometric discontinuity at the corner of a square section specimen generates easier cyclic slip than that on a flat specimen surface [35]. The fracture surface determines a mixed mode fracture morphology, consistent with other studies [36,37]. The crack origin shows intergranular cracking usually from a large subsurface grain. The surface shows flat transgranular cracking planes with a characteristic river pattern propagating radially. The early crack propagation reveals a shallow microplastic strain wave pattern. The visible anodic coating formed from alumina is 8 μm in thickness.

The propagation region shows a “rock candy” fracture pattern. The selected areas representing transgranular cracking occurs through several material grains characterized by shear grades, river patterns, and tongues (Fig. 8(d)). Figure 8(e) shows the fracture surfaces in the propagation and final failure region. The fatigue crack growth rate determines the visible increase in the width of fatigue striations. In the region of slow and stable

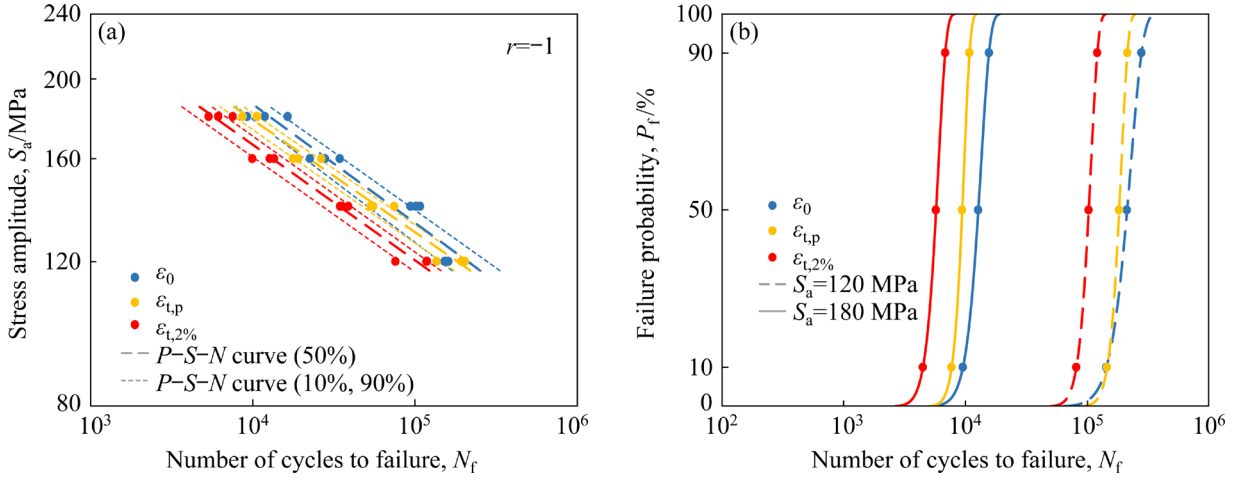

Fig. 7 Experimental results of high-cycle fatigue tests for EN AW 6063 T66 alloy: (a) *P*−*S*−*N* curves; (b) Weibull cumulative distribution function for stress amplitudes of 120 and 180 MPa

Table 3 *P*−*S*−*N* curve approximation results for Weibull distribution

Specimen	Stress amplitude, S_a/MPa	Weibull distribution			Failure probability, P_f/%	Number of cycles, N_f
		Location parameter, λ	Shape parameter, α	Scale parameter, δ		
ε_0	180	2.86	17.57	1.27	10	9491
					50	12699
					90	15550
	120	3.67	17.35	1.69	10	142698
					50	211190
					90	277475
$\varepsilon_{t,p}$	180	3.02	19.66	0.97	10	7675
					50	9377
					90	10765
	120	4.15	20.25	1.13	10	144927
					50	181857
					90	212575
$\varepsilon_{t,2\%}$	180	2.67	17.97	1.11	10	4460
					50	5722
					90	6803
	120	4.02	17.38	1.01	10	80972
					50	102311
					90	120406

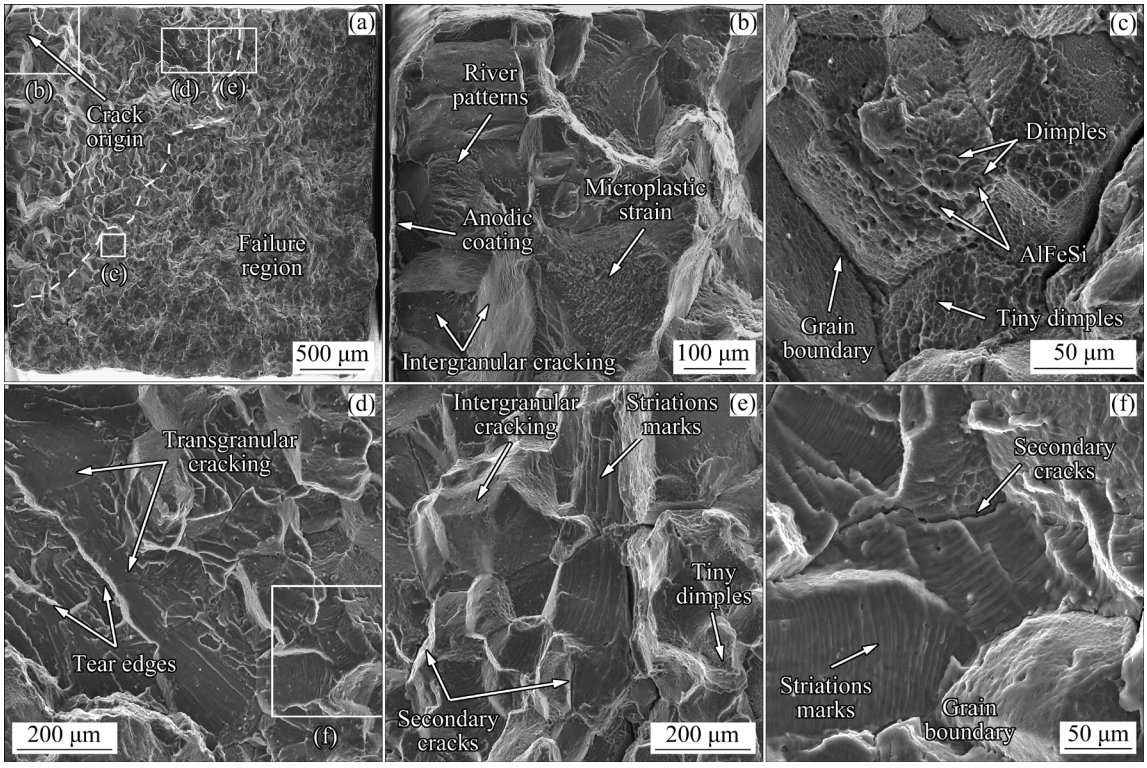

Fig. 8 Fatigue fracture surface of as-received EN AW 6063 T66 alloy (S_a=180 MPa, N_f=11879): (a) General view; (b−f) Corresponding magnified images of regions in (a)

crack growth, intergranular secondary cracks occur. Figure 8(f) reveals overlapping pockets of plastic fatigue striations forming a wave pattern. Subsequently, the crack is intergranularly continuous according to the grain boundary orientation.

The boundary criterion of the crack propagation region and plastic fracture is the area of ductile fracture surface morphology. Figure 8(c) shows a normal fracture formed by plastic decohesion. The characteristic dimples with different dimensions formed by the uniaxial loading of the tensile cycle phase are visible. The observed AlFeSi precipitates cause local stress concentration. The size of dimples is correlated with the distance between the precipitates and their size [35]. The figure contains evidence of intergranular plastic fracture with smaller size and depth tiny dimples formed due to separation at the grain boundary.

Figure 9 shows SEM micrographs of the material fracture surface for 2% pre-strain. The specimen tested at a stress amplitude of 180 MPa survived a number of cycles to failure of 5350. The fracture surface shows the same three areas of the as-received material (Fig. 9(a)). The fracture morphology shows an increased level of the characteristic intergranular cracking (Fig. 9(b)). The fracture surface is more susceptible to grain boundary failure (Fig. 9(c)). The intergranular cracking is formed for lower surface energy of grain boundaries than the energy in the cleavage plane. This type of fracture is supported by visible AlFeSi precipitates accumulated at grain boundaries. The transgranular cracking shows a reduced area with a small number of common grains. The monotonic strain generates areas of dislocation accumulation in the neighbourhood of grain boundaries [38,39]. The increase in dislocation density and tendency to slip bands is not restrained under cyclic loading. The phenomenon depends on the strain level. The dislocation distribution of as-received material is more uniform. The monotonic damage is the first failure mechanism, significantly determining the fatigue life. The observed number of secondary cracks seems to be less than that of the as-received material. The energy dissipation during the initiation of these cracks can result in delayed propagation of the primary fatigue crack [40]. The saturation of strain damage determines the fatigue crack initiation and propagation process. A decrease in fatigue life is observed for the pre-strained material at the same stress amplitude.

3.4 Fatigue life prediction

The nonlinearity of the numerical model determines the necessity of selecting boundary conditions for the internal bending radius of the profile R_p of 2150 mm. A series of calculations with a variable value of the roll displacement f_r were conducted. The data approximation to a regression model allowed the estimation of the model input parameters. A profile bending consistent with the real object was obtained.

The results of the numerical model are dependent on the location of the data read. To provide evidence of the variations, Fig. 10 shows the response of the profile to the applied displacement as a function of time. The normalized force in the roll increases according to the displacement. When the initial extremum of the function is achieved, a decrease in force is observed with an increase in roll displacement. The model

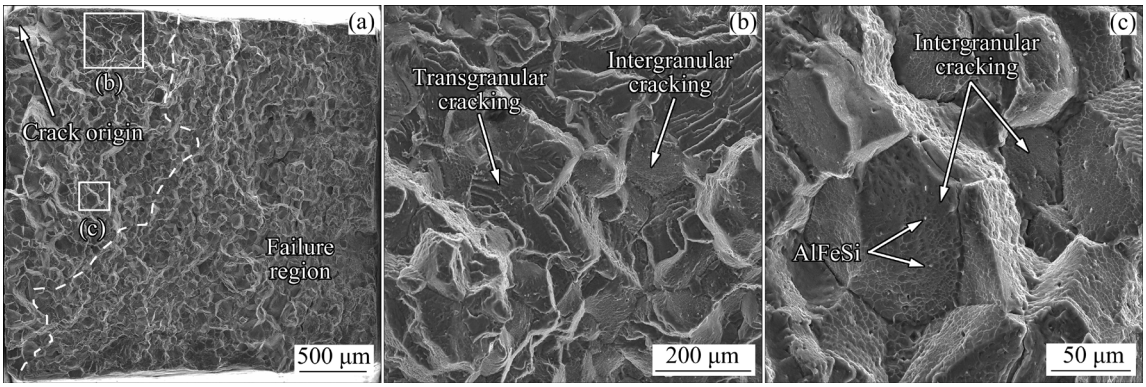

Fig. 9 Fatigue fracture surface of 2% tensile pre-strained EN AW 6063 T66 alloy (S_a=180 MPa, N_f=5350): (a) General view; (b, c) Corresponding magnified images of regions in (a)

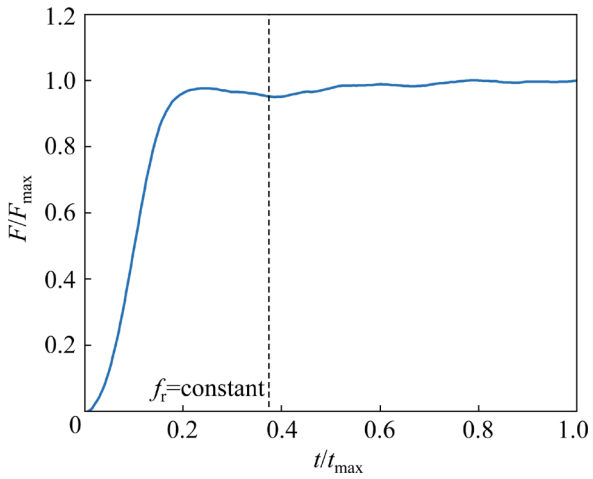

Fig. 10 Bending roller force of profile

response indicates a decrease in local stiffness until the maximum displacement is achieved (vertical dotted line). A further increase in force is noted until the conditions finally stabilize at about the midpoint of the simulation. The analysis of the dimensions and shape profile indicates a slightly larger deformation in the bending region immediately behind the straight section. The identified discontinuities are also present in the real profile. The obtained matches suggest the correctness of the proposed conditions for the numerical simulation of the roller bending.

Figure 11 shows a normal stress distribution map of the profile. To avoid the possible effect of the initial plastic formation mechanisms indicated in the previous paragraph, the results presented are for a selected time in the second half of the simulation. A similar algorithm was used to select the sampling site for the experimental tests. The projection on the x−z plane shows the visible part of the profile and the upper roll. The plasticization of the material occurs in the support region due to the applied bending moment. The maximum values are located in the extreme fibres. The higher values were observed in the compression region. The non-uniform distribution of stress can result in disproportionate deformation of the profile section.

The input data of the fatigue life distribution prediction model apply the results of numerical analysis (a calculated strain of 0.9% for stress 237.8 MPa) and experimental P−S−N curves for as-received material (Table 3, ε_0) and 2% pre-strained material (Table 3, $\varepsilon_{t,2\%}$). The output data are estimated P−S−N curves for the material sampled from the profile tensile region ($\varepsilon_{t,p}$). The correlation of the number of cycles and pre-strain level was approximated by least squares linear regression. Figure 12 shows the results for two levels of stress amplitude and variable failure probability. The data are determined by a probabilistic approach assuming the estimation of fatigue life distributions, according to Eq. (1). The points are consistent with the experimental data described in Section 3.2. The dashed line corresponds to the numerically calculated local strain of the profile for the predicted data.

Figure 13 shows a graphical visualization of the Weibull cumulative distribution function for stress amplitude of 180 and 120 MPa. The points are experimental values for the selected failure probability P_f. The solid line represents the distribution result, according to Fig. 7(b). The data prediction for any pre-strain was carried out for the cumulative Weibull distribution and the curve in Fig. 12. The figure shows that the model predictions (dashed line) are in good agreement with the experimental results for probabilistic scatter bands. Table 4 contains the fatigue life estimation results

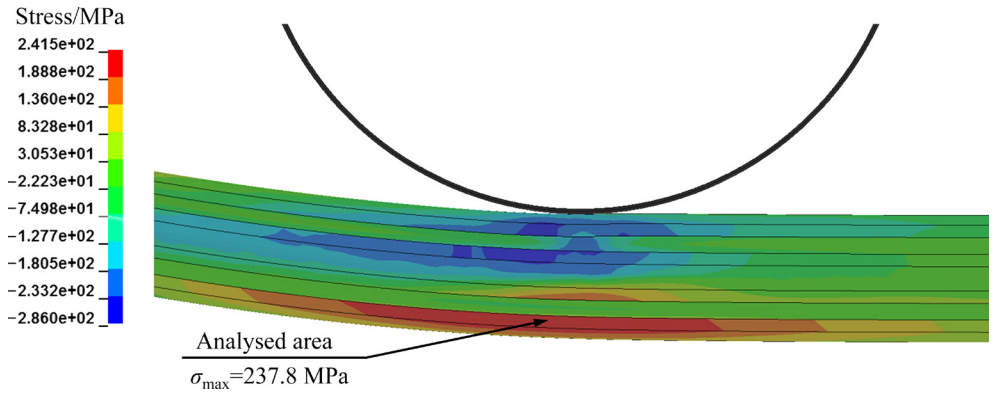

Fig. 11 Normal stress distribution in x−z plane after numerical roller bending

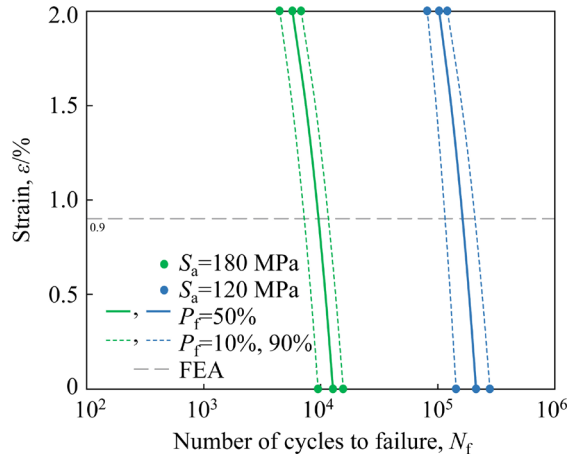

Fig. 12 Fatigue life estimation curves of two stress amplitude levels for tensile strain

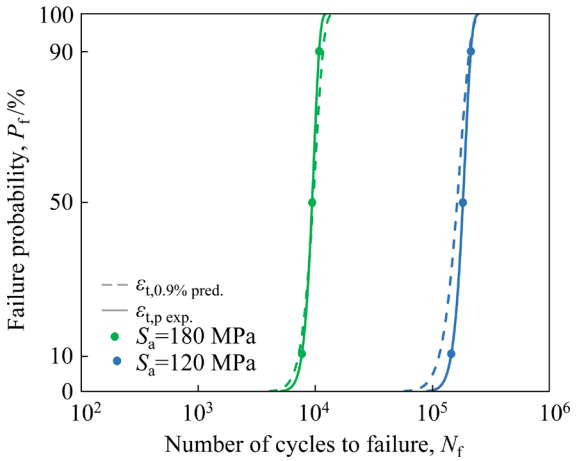

Fig. 13 Weibull cumulative distribution function of experimental and predicted fatigue life for 0.9% tensile strain

Table 4 Experimental results and predicted values of fatigue life

S_a/ MPa	P_f/ %	N_f	$N_{f,pred.}$	Relative error/%
180	10	7675	7227	−5.8
	50	9377	9559	1.9
	90	10765	11614	7.8
120	10	144927	114921	−20.7
	50	181857	162194	−10.8
	90	212575	206794	−2.7

for selected failure probabilities and relative error. The analytical values ($N_{f,pred.}$) are close to the experimental fatigue life (N_f). The average estimation error is equal to 7.4%. The negative error values determine the predicted fatigue life below the experimental values. For these results, the model provides safe results. A larger spread of errors is seen for extreme values of failure probability. The prediction accuracy of model can be improved by testing experimentally pre-strained levels close to the numerical strain of 0.9%.

4 Conclusions

(1) The profile forming determines noticeable local variations in the mechanical behaviour of the EN AW 6063 T66 aluminium alloy. The strain hardening is characterised by an increase in tensile strength of 2.6% compared to the as-received material. The profile deformation significantly affects the yield strength. An increase of 5.9% was observed in the material sampled from the tensile region. A similar trend is determined for the exponent of the Ramberg-Osgood model.

(2) The cyclic behaviour in stress-controlled fatigue tests shows a decrease in the fatigue life distribution for the high plastic strain. The scale parameter of the Weibull distribution decreases with the level of pre-strain. Given the noticeable variations in the results, it should be assumed that the cyclic behaviour of the material is significantly affected by the failure mechanism generated under static damage.

(3) The fractographic analysis showed a mixed mode fracture morphology. The pre-strain determines an increased level of grain boundary cracking than transgranular cracking. The effect of tensile static strain determines the dislocation accumulation in the neighbourhood of grain boundaries resulting in faster failure. The observed variation on the fracture surface correlates with a decrease in fatigue life.

(4) The results of numerical simulation of roller bending and experimental *P*–*S*–*N* curves provided a prediction of the Weibull distribution for the selected material plastic strain. The average estimation error for experimental and predicted fatigue life is 7.4%. The results show a good correlation between the probabilistic scatter bands. The model can be implemented for other strain levels, not exceeding the tested pre-strain.

Acknowledgments

The research is co-financed by the European Regional Development Fund under NCBR

POIR.04.01.04-00-0006/19 grant, “Cross-belt system for automated sorting of unit loads by a two-stage method”, performed in 2019-2022.

References

[1] BANABIC D. Advanced methods in material forming [M]. Berlin: Springer, 2007.

[2] HUA M, BAINES K, COLE I M. Bending mechanisms, experimental techniques and preliminary tests for the continuous four-roll plate bending process [J]. Journal of Materials Processing Technology, 1995, 48: 159−172.

[3] WELO T, WIDERØE F. Precision bending of high-quality components for volume applications [J]. Transactions of Nonferrous Metals Society of China, 2010, 20(11): 2100−2110.

[4] FENG Z K, CHAMPLIAUD H. Modeling and simulation of asymmetrical three-roll bending process [J]. Simulation Modelling Practice and Theory, 2011, 19: 1913−1917.

[5] YANG G, MORI K, OSAKADA K. Determination of forming path in three-roll bending using FEM simulation and Fuzzy reasoning [J]. Journal of Materials Processing Technology, 1994, 45: 161−166.

[6] SHIM D S, KIM K P, LEE K Y. Double-stage forming using critical pre-bending radius in roll bending of pipe with rectangular cross-section [J]. Journal of Materials Processing Technology, 2016, 236: 189−203.

[7] HUDOVERNIK M, STAUPENDAHL D, GHARBI M, HERMES M, TEKKAYA A E, KUZMAN K, SLABE J M. 3D numerical analysis of 2D profile bending with the torque superposed spatial bending method [J]. Journal of Mechanical Engineering, 2013, 59(3): 139−147.

[8] CHIEW S P, JIN Y F, LEE C K. Residual stress distribution of roller bending of steel rectangular structural hollow sections [J]. Journal of Constructional Steel Research, 2016, 119: 85−97.

[9] ESMAEILI S, WANG X, LLOYD D J, POOLE W J. On the precipitation-hardening behavior of the Al−Mg−Si−Cu alloy AA6111 [J]. Metallurgical and Materials Transactions A, 2003, 34: 751−763.

[10] CHAKRABARTI D J, LAUGHLIN D E. Phase relations and precipitation in Al−Mg−Si alloys with Cu additions [J]. Progress in Materials Science, 2004, 49: 389−410.

[11] AYDI L, KHLIF M, BRADAI C, SPIGARELLI S, CABIBBO M, EL MEHTEDI M. Mechanical properties and microstructure of primary and secondary AA6063 aluminium alloy after extrusion and T5 heat treatment [J]. Materials Today: Proceedings, 2015, 2: 4890−4897.

[12] OZTURK F, ESENER E, TOROS S, PICU C R. Effects of aging parameters on formability of 6061-O alloy [J]. Materials and Design, 2010, 31: 4847−4852.

[13] WANG Y J, LIAO H C, WU Y N, YANG J. Effect of Si content on microstructure and mechanical properties of Al−Si−Mg alloys [J]. Materials and Design, 2014, 53: 634−638.

[14] XU Y, ZHAN L, LI W. Effect of pre-strain on creep aging behavior of 2524 aluminium alloy [J]. Journal of Alloys and Compounds, 2017, 691: 564−571.

[15] DINH K A, HONG S T, CHOI S J, KIM M J, HAN H N. The effect of pre-strain and subsequent electrically assisted annealing on the mechanical behaviors of two different aluminium alloys [J]. International Journal of Precision Engineering and Manufacturing, 2020, 21: 2345−2358.

[16] WERBER A, LIEWALD M. Influence of pre-strain and heat treatment on mechanical properties of aluminum sheet [J]. International Journal of Material Forming, 2012, 5: 307−315.

[17] AL-RUBAIE K S, DEL GRANDE M A, TRAVESSA D N, CARDOSO K R. Effect of pre-strain on the fatigue life of 7050-T7451 aluminium alloy [J]. Materials Science and Engineering A, 2007, 464: 141−150.

[18] BRANCO R, COSTA J D, BORREGO L P, WU S C, LONG X Y, ANTUNES F V. Effect of tensile pre-strain on low-cycle fatigue behaviour of 7050- T6 aluminium alloy [J]. Engineering Failure Analysis, 2020, 114: 104592.

[19] KIM J, KANG J W, LEE D E, KIM D Y. Methodology for evaluation of residual stress effect on small corner-crack initiation and growth [J]. Materials, 2019, 12(18): 2904.

[20] FROUSTEY C, LATAILLADE J L. Influence of large pre-straining of aluminium alloys on their residual fatigue resistance [J]. International Journal of Fatigue, 2008, 30: 908−916.

[21] EN 573-3:2019. Aluminium and aluminium alloys. Chemical composition and form of wrought products. Chemical composition and form of products.

[22] PANIGRAHI S K, JAYAGANTHAN R, PANCHOLI V. Effect of plastic deformation conditions on microstructural characteristics and mechanical properties of Al 6063 alloy [J]. Materials and Design, 2009, 30: 1894−1901.

[23] ADAMCZYK-CIEŚLAK B, MIZERA J, KURZYDŁOWSKI K J. Microstructures in the 6060 aluminium alloy after various severe plastic deformation treatments [J]. Materials Characterization, 2011, 62: 327−332.

[24] ASTM E112. Standard test methods for determining average grain size [S].

[25] ISO 6892-1. Metallic Materials-Tensile Testing—Part 1: Method of Test at Room Temperature [S].

[26] ISO — 1099. Metallic Materials-Fatigue Testing — Axial Force- Controlled Method [S].

[27] ISO—12107. Metallic Materials-Fatigue Testing—Statistical Planning and Analysis of Data [S].

[28] TOMASZEWSKI T, SEMPRUCH J. Determination of the fatigue properties of aluminium alloy using mini specimen [J]. Fatigue Failure and Fracture Mechanics, 2012, 726: 63−68.

[29] SOKOLOV M A, LUCON E. Small specimen test techniques [M]. West Conshohocken, PA, USA: ASTM International, 2015.

[30] TOMASZEWSKI T, SEMPRUCH J. Fatigue life prediction of aluminium profiles for mechanical engineering [J]. Journal of Theoretical and Applied Mechanics, 2017, 55(2): 497−507.

[31] FANG J, LIANG C, LU S Q, WANG K L. Effect of geometrical parameters on forming quality of high-strength TA18 titanium alloy tube in numerical control bending [J]. Transactions of Nonferrous Metals Society of China, 2018,

28(2): 309−318.
[32] LI H, YANG H, ZHAN M, GU R-J. Forming characteristics of thin-walled tube bending process with small bending radius [J]. Transactions of Nonferrous Metals Society of China, 2006, 16(2): 613−623.
[33] EN 1999-1-1. Eurocode 9: Design of Aluminium Structures —Part 1-1: General Structural Rules [S]. Belgium: European Committee for Standardization, 2007.
[34] WEIBULL W. A statistical theory of the strength of materials [M]. Stockholm: Generalstabens Litografiska Anstalts Förlag, 1939.
[35] KOCAŃDA S. Fatigue failure of metals [M]. Poland: WNT, 1978.
[36] SUNDSTRÖM R. High cycle fatigue properties of extruded 6060-T6, 6063-T6 and 6082-T6 [M]. Sweden: KTH, 2018.
[37] NANNINGA N E. High cycle fatigue of AA6082 and AA6063 aluminum extrusions [M]. Michigan: Michigan Technological University, 2008.
[38] WHITTAKER M T, EVANS W J. Effect of pre-strain on the fatigue properties of Ti834 [J]. International Journal of Fatigue, 2009, 31: 1751−1757.
[39] LI J, ZHANG P, LU L, LV F, MIAO X T, CHANG L, ZHOU B B, HE X H, ZHOU C Y. Effect of pre-strain on fatigue crack growth behavior for commercial pure titanium at ambient temperature [J]. International Journal of Fatigue, 2018, 117: 27−38.
[40] SURESH S. Fatigue of materials [M]. 2nd ed. Cambridge: Cambridge University Press, 1998.

辊弯成形下塑性应变对挤压态 6063 T66 铝合金型材疲劳性能的影响

Tomasz TOMASZEWSKI, Michał STOPEL, Andrzej SKIBICKI, Jan SEYDA, Tomasz PIĄTKOWSKI

Faculty of Mechanical Engineering, Bydgoszcz University of Science and Technology, Bydgoszcz, Poland

摘　要：分析从辊弯成形型材区和预应变材料取样的材料的拉伸塑性应变。利用概率 Weibull 累积分布(*P*−*S*−*N* 曲线)近似高周疲劳的实验数据。利用 LS-Dyna 程序和实验数据对辊弯成形进行数值模拟，建立疲劳寿命预测模型。材料的循环行为表明，随着静态失效水平的增加，疲劳寿命分布减小。断裂表面的断口形貌分析表明，由于晶界附近的位错积累，拉伸预应变的晶间裂纹水平增加。所提模型预测结果与概率散射带具有良好的相关性 (误差低于 10%)。

关键词：6063 铝合金；预应变；高周疲劳；*P*−*S*−*N* 曲线；Weibull 分布

(Edited by Xiang-qun LI)